

Petrological evidence for deep subduction of organic carbon to subarc depths

Han Hu ¹, Lifei Zhang ¹✉, Chunyuan Lan ¹ & Zhicheng Liu ¹

The significance of subducted organic carbon for the deep carbon cycle has been demonstrated by the presence of ultra-deep diamonds and arc emissions. However, there is no convincing evidence that organic carbon can be subducted to subarc depths. This study provides the evidence for deep subduction of sedimentary organic carbon to mantle depths through petrological observation, Raman and isotopic analyses of ultrahigh-pressure (UHP) coesite- and graphite-bearing pelitic schists. The analyzed graphite shows light $\delta^{13}\text{C}$ values (-24.7 to -22.5%), indicating a sedimentary organic carbon source. Petrological characteristics of graphite co-existing with coesite in garnet and P-T calculations suggest that organic graphite was subducted to the subarc depths exceeding 90 km. This research represents the petrological evidence for the deep subduction of organic carbon to mantle depths and may provide insight into the origin of diamonds with light $\delta^{13}\text{C}$ values and contribute as key evidence for the Lomagundi event.

¹Key Laboratory of Orogenic Belts and Crustal Evolution, School of Earth and Space Sciences, Peking University, Beijing 100871, China. ✉email: Lfzhang@pku.edu.cn

Oceanic sediments constitute a substantial carbon source within subduction zones, encompassing both inorganic and organic carbon components that are transported into the subduction factory. Understanding the fate of these carbon inputs in subduction zones is crucial for gaining insights into the global carbon cycling throughout Earth's history. While the significance of carbonate in the subduction-zone carbon cycle has been extensively investigated in recent decades^{1–3}, the importance of organic carbon within subduction-zone lithologies and deep fluids has been relatively overlooked^{4,5}. The deep subduction of reduced organic carbon has impacts on various geological events, including the Great Oxygenation Event⁶, the Lomagundi event⁷, arc carbon isotopic signature⁸, and the formation of deep diamonds with light carbon isotopic features⁹.

Diamond provides the principal data source for investigating mantle carbon. Low $\delta^{13}\text{C}$ values (ranges from -40 to $+3\text{‰}$, with peak values of -6‰) in eclogitic diamonds, along with higher-than-mantle $\delta^{18}\text{O}$ values in their silicate inclusions, suggest the potential contributions of deeply subducted organic carbon into the mantle^{10,11}. Similarly, the relatively light carbon isotope composition ($\delta^{13}\text{C}$ ranges from -29 to -18‰) of ophiolite-hosted diamonds indicates the possible contribution of subducted biogenic carbon⁹. Kimberlite, a common host lithology of diamonds, also offers insights into mantle carbon. The lower $\delta^{13}\text{C}$ ratios of carbonate-rich hypabyssal kimberlites from the Mesozoic onwards (<250 Ma) suggest that subduction of organic carbon into the deep mantle, following the Cambrian Explosion when organic carbon deposition in marine sediments increased significantly¹². While these findings suggest the potential subduction of surface-derived organic carbon into the deep mantle, they lack petrological evidence to confirm the deep subduction of organic carbon.

Here, we present robust petrological evidence to support the subduction of surficial organic carbon to mantle depths, which may contribute to the formation of (ultra-) deep diamonds with light $\delta^{13}\text{C}$ values and potentially offer an explanation for the Lomagundi event through the increased subduction of organic carbon.

Results and discussion

Petrography and mineral chemistry of graphite-bearing pelitic schists. The studied Tianshan graphite-bearing pelitic schists (Supplementary Note 1 and Supplementary Fig. 1) are well-foliated, with phengite defining the foliation. These schists consist of white mica (phengite 25% and paragonite 10%), garnet (10%), quartz (25%), retrograde albite (25%), and graphite ($<5\%$); rutile, epidote/zoisite, apatite, tourmaline, chlorite, carbonate and titanite/ilmenite occur in minor amounts. Modal abundances were estimated through visual observation.

Garnet occurs as subhedral to euhedral crystal, measuring around 0.1 – 0.5 mm in size (Fig. 1a–d), and some garnets are fractured. Obvious compositional zonation can be observed in these garnets (Fig. 1e, f and Supplementary Data 1). From core to rim, X_{Grs} (mineral abbreviations refer to Supplementary Note 2) increases from 0.08 to 0.24 , X_{Prp} remains constant at about 0.14 , and X_{Sps} and X_{Alm} decrease from 0.03 to 0.01 and 0.77 to 0.62 , respectively. Graphite, rutile, and occasionally coesite are included in these garnet crystals (Figs. 1b–d and 2a–d). There are also some atoll-shaped garnets in the samples, whose irregular shell structure encircles cores partially or entirely replaced by phengite, epidote, and quartz. The “shell” of atoll-shaped garnets shows a composition similar to the rim of complete garnet crystals. No fluid inclusions were observed in the garnet crystals of the studied pelitic schists.

Phengite grains in the matrix measure around 50 – 150 μm in width (Fig. 1a, c) and have a Si content of 3.34 – 3.42 atoms per formula unit (apfu; Supplementary Data 1). The phengite filling in the core of the atoll-shaped garnet shows a Si content of 3.39 – 3.45 apfu. Paragonite has a grain size of 100 – 300 μm in width, coexisting with phengite or quartz. Paragonite shows steady Na content (0.67 – 0.75 apfu) and K content (0.04 – 0.08 apfu).

Graphite grains are dispersed throughout the investigated pelitic schists (Fig. 1a, b) and are included in garnet, phengite, and quartz (Fig. 1c, d), as well as paragonite, albite, titanite, and tourmaline in some cases. Notably, minute graphite inclusion commonly trails extend parallel to the crystal faces of garnet at discrete growth stages (Fig. 1b–d), and rutile inclusions are also included in these graphite trails.

UHP metamorphism of graphite-bearing pelitic schists. The identification of coesite inclusions within garnet (Fig. 2a–f) in the studied pelitic schists provides compelling evidence for UHP metamorphism of the metasedimentary rocks in the Tianshan orogenic belt. This finding is in agreement with previously published literature^{13,14}. Two coesite crystals were identified in the garnet, which contains quartz with radial fractures (Fig. 2a, b). The monomineralic coesite (Coe-1) displays a well-characterized strong coesite band at 521 cm^{-1} , with no quartz bands observed (Fig. 2a–e). The good preservation of this small coesite grain can be explained by its size, which was too small to cause remarkable fractures in the rigid host garnet during decompression. This is further evidenced by the weak radial fractures surrounding Coe-1 (Fig. 2c and insert figure in Fig. 2e). Another coesite crystal (Coe-2) shows a strong band at 521 cm^{-1} . Additionally, relatively weak quartz bands at 467 and 205 cm^{-1} are visible (Fig. 2a, b, d, f), potentially indicating the partial transformation of coesite to quartz during the decompression process.

The P–T pseudosection of the graphite-bearing pelitic schist H1813B reveals a roughly isothermal decompression path (Fig. 3a). Garnet core composition plots in the field of Grt + Omp + Phn + Cld + Amph + Lws + Qz/Coe + Rt, highlighting a peak pressure stage at 28 kbar and 540°C (M1 stage). These values may imply UHP metamorphism and concur with the measured and projected phengite compositions (Si = 3.34 – 3.45 apfu; Fig. 3b), matching with the well-preserved small coesite inclusions in garnet.

Carbon source of graphite. Previous kinetic studies^{15,16} have indicated that the carbon diffusion in graphite is very sluggish, implying that well-crystallized graphite is isotopically inert and does not undergo isotopic alteration during subsequent hydrothermal alteration, even under high P–T conditions. Metamorphic graphite derived from biogenic carbon commonly shows light isotopic signatures with a mean $\delta^{13}\text{C}$ of around -25‰ ¹⁷. This signature is quite homogeneous for a set of grains derived from the same organic precursor and formed under the same metamorphic grade¹⁸. In contrast, fluid-deposited graphite shows a wide range of carbon isotopic signatures¹⁹, depending on both the origin of carbon (e.g., $<-20\text{‰}$ for unmetamorphosed marine organic matter, $-5 \pm 2\text{‰}$ for mantle carbon¹⁸ and $0 \pm 2\text{‰}$ for marine carbonates²⁰) and the genetic mechanisms involved in its precipitation, such as the evolution of the carbonic fluid with time²¹.

The total organic carbon (TOC) concentration in the studied coesite- and graphite-bearing pelitic schists ranges from 0.31 to 1.22 wt.% (Supplementary Data 2). These pelitic schists have homogeneous $\delta^{13}\text{C}_{\text{TOC}}$ values of -24.7 to -22.5‰ , which fall in the range of typical marine organic matter (Fig. 4; Supplementary

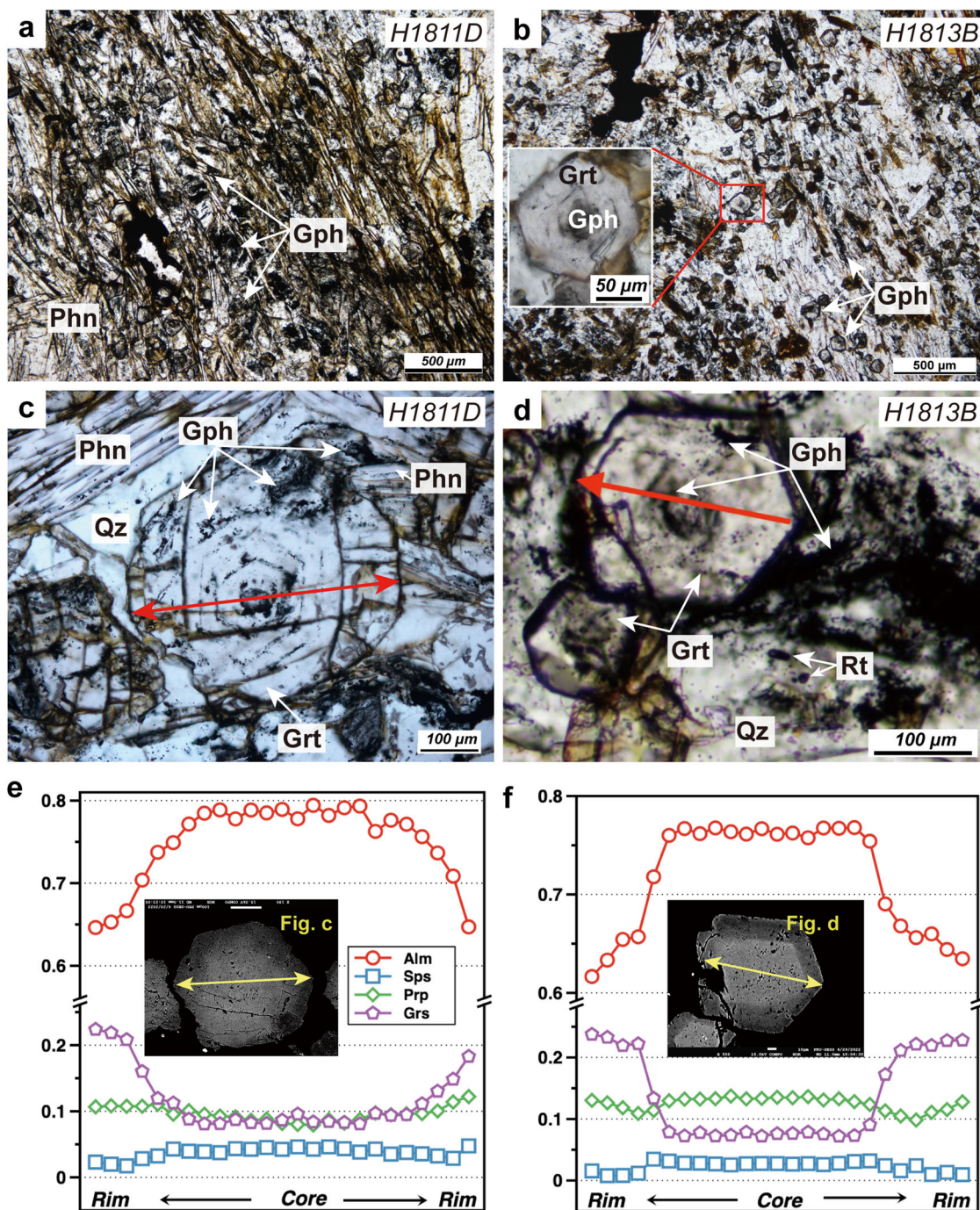


Fig. 1 Representative photomicrographs and mineral compositions of the studied graphite-bearing pelitic schists from Tianshan, China. **a** and **b** Representative photomicrographs (plane-polarized light) of graphite (Gph)-bearing pelitic schists, which are mainly composed of phengite (Phn), quartz (Qz), and garnet (Grt), with minute graphite in phengite, quartz, and garnet. **c** and **d** Representative photomicrographs (plane-polarized light) of graphite inclusion, which trails along crystal faces highlighting growth zones of garnet, and rutile (Rt) is included in the matrix quartz. **e** and **f** Backscattered electron images and chemical composition profiles of garnets in **c** and **d**.

Data 2). The $\delta^{13}\text{C}_{\text{TOC}}$ of picked graphite-bearing garnet crystals and picked graphite-bearing whitemica (phengite and paragonite) are in agreement with that of the bulk rock (Fig. 4 and Supplementary Data 2). This consistency suggests that graphite serves as the primary organic carbon phase in these samples. These isotopic data are close to the $\delta^{13}\text{C}_{\text{TOC}}$ values of organic matter found in iron deposits from the western Tianshan (-25.2% ; Fig. 4)²², suggesting a surface-derived organic carbon source for the studied graphite (Fig. 4 and Supplementary Data 2).

Formation of graphite. In subduction zones, graphite can be formed by the transformation of organic matter during metamorphism (metamorphic graphite) or by precipitation from carbon-bearing fluids (fluid-deposited graphite)^{19,23}.

The studied graphite occurs as minute solid inclusion tracks along crystal faces of garnet at each growth stage (Fig. 1b–d). There are two hypotheses for the formation of this graphite: (i) graphite precipitated from a carbonic fluid during garnet crystallization, and (ii) pre-existing graphite was included by the garnet during its crystallization.

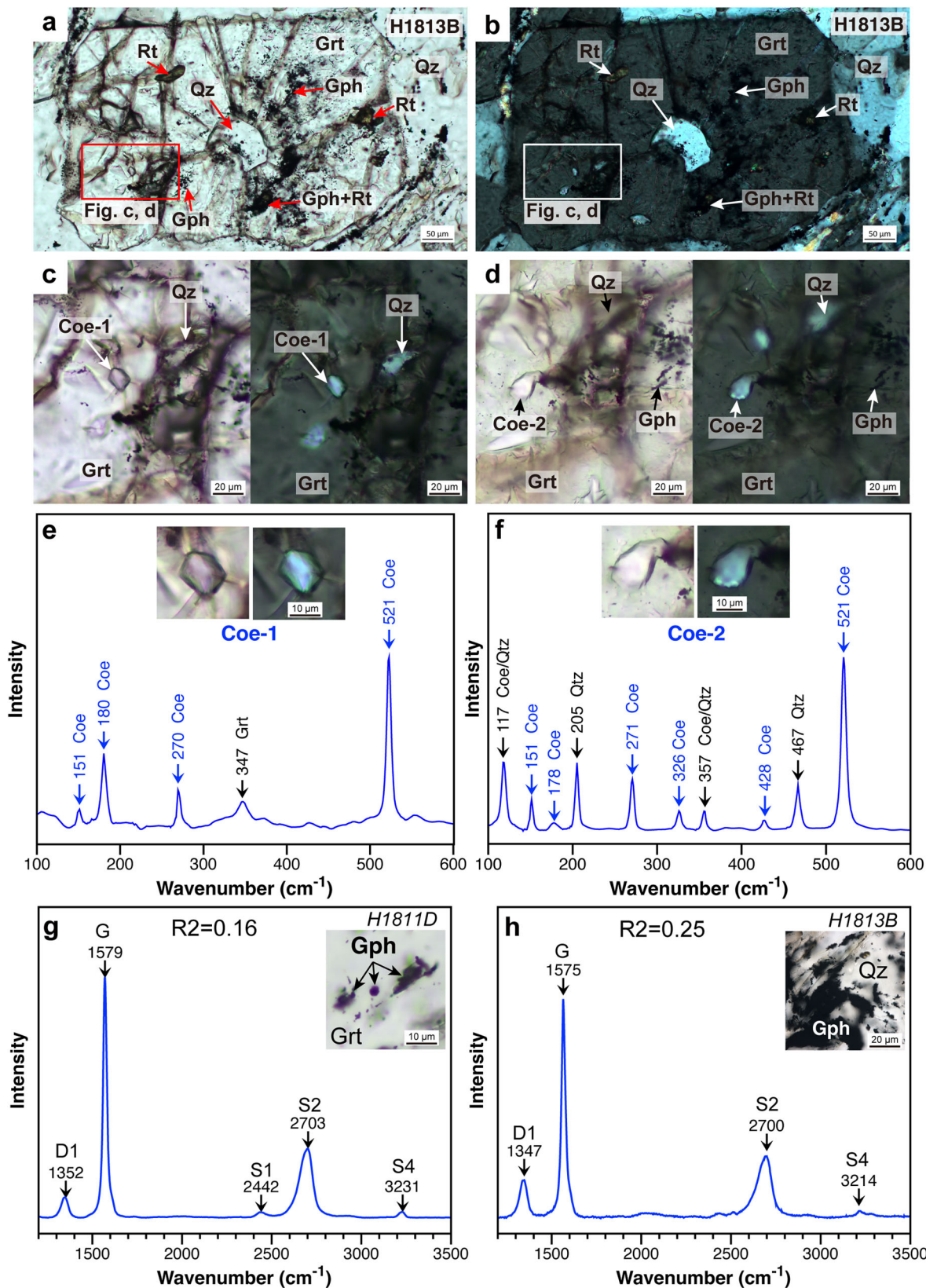


Fig. 2 Coesite and graphite inclusions in garnet. **a** and **b** Two coesite (Coe) crystals were found in the garnet (Grt), which contains quartz (Qz) with radial fractures. Graphite (Gph) and rutile (Rt) are contained in garnet. **a** and **b** are plane- and cross-polarized light, respectively. **c** and **d** Coesite inclusions in garnet. Plane- and cross-polarized light. **e** and **f** Raman spectra of Coe-1 and Coe-2 in garnet. **g** and **h** Raman spectra of graphite in garnet and quartz.

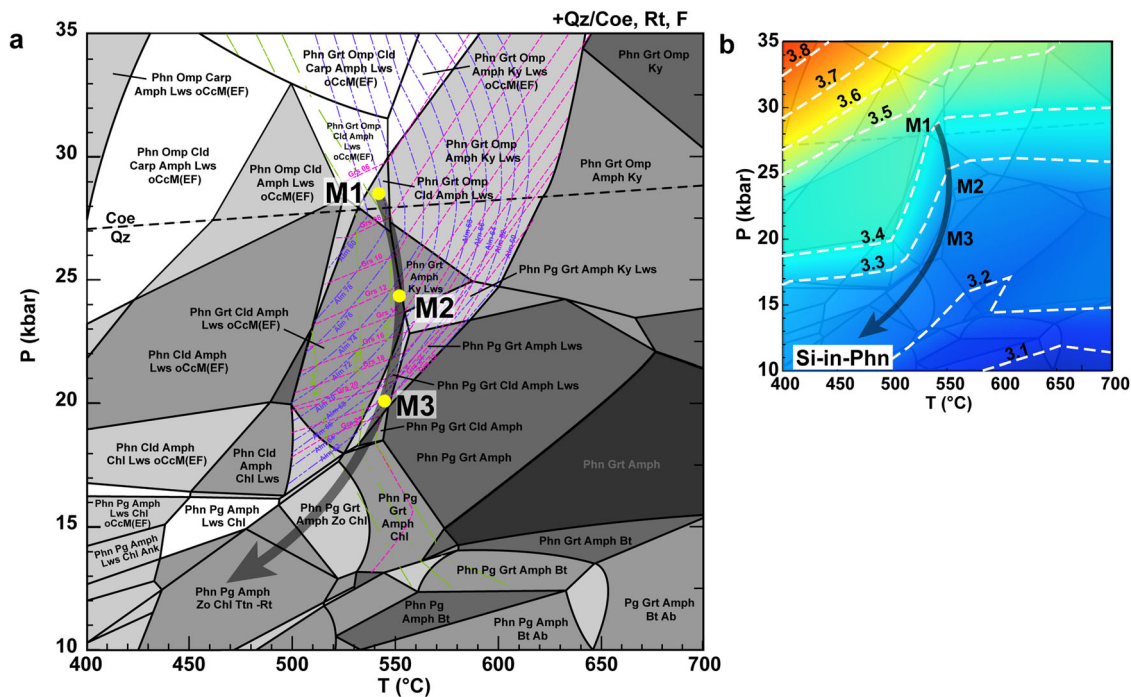


Fig. 3 P-T phase diagram together with Si in phengite isopleths for bulk H1813B. **a** P-T pseudosection for the investigated coesite- and graphite-bearing UHP pelitic schist (sample H1813B) from the Chinese southwestern Tianshan HP–UHP metamorphic belt, system NCKFMASHTi+CO₂ (+ quartz/coesite + rutile + F) based on the XRF bulk composition from Supplementary Data 3. X_{Prp} , X_{Grsr} , and X_{Alm} isopleths in garnet were plotted in green, pink, and purple dashed lines, respectively. The gray curved line is the constrained P-T path for the exhumation of H1813B. M1, M2 and M3 stages are constrained by the composition of garnet core, mantle and rim, respectively. **b** Phengite Si-content isopleths (apfu).

Regarding the first hypothesis for the formation of graphite in the studied sample, it is plausible that the graphite precipitated from either CO₂- or CH₄-bearing metamorphic fluids. The former can be ruled out because the graphite precipitated from sedimentary carbonate-sourced COH fluids generally shows high $\delta^{13}\text{C}$ values of around 0‰²⁴ in Alpine Corsica or around –13‰²⁵ in the Chinese Tianshan (Fig. 4). Conversely, biotic (thermogenic) CH₄-bearing fluids could potentially be the source of graphite in these samples, given the low $\delta^{13}\text{C}$ value (<–20‰) associated with biotic CH₄²⁶. Although carbonaceous matter in subducted sediments can release biotic CH₄, forming carbonic fluids with low $\delta^{13}\text{C}$ during the thermal maturation stage at temperatures between 200 and 300 °C, these slab-released CH₄ fluids would tend to go upwards rather than go down with the slab to the deep subarc depths (as indicated by coesite inclusions representing UHP conditions). This makes the CH₄ fluid deposition hypothesis less plausible. Furthermore, the graphite trails observed in our study do not correspond to chemical zones in garnet (Fig. 1c–f), further diminishing the likelihood of the fluid deposition hypothesis. Hence, we think the first hypothesis (fluid deposition) is less possible in our study.

According to the published literature, the degree of metamorphic graphite crystallization linearly correlates with the peak temperature experienced during metamorphism²⁷. Raman spectroscopy is an effective tool for evaluating the crystallization degree of graphite and its relationship to the metamorphic degree²⁸. In this study, graphite shows a sharp peak at the G band (around 1580 cm⁻¹) with a small peak at the D1 band (around 1350 cm⁻¹) in the first-order region, and D2 (around 1620 cm⁻¹) is inseparable (Fig. 2g, h). In the second-order region, S1 (~2450 cm⁻¹), S2 (~2700 cm⁻¹), and S4 (~3200 cm⁻¹) peaks were observed. The R2 ratio²⁹ of graphite, defined as the D1/(G + D1 + D2) peak area ratio, varies from 0.16 to 0.37, with the majority falling between 0.2 and 0.3. The Raman spectrum of the

studied graphite is comparable to that of metamorphic graphite formed at ~540 °C in the European Alps²⁷. Since the T_{max} in this study is around 550 °C (M1 stage in Fig. 3a), it suggests that graphitization might be a possible mechanism for graphite formation in this study. Additionally, the similar R2 ratio of graphite crystals in garnet at each growth stage indicates that these graphite trails underwent a consistent peak metamorphic temperature. It is suggested that the graphite was transformed from disordered organic carbon via solid-state transformation (graphitization) in sediments with increasing subduction temperature. The graphitized organic carbon grains were then contained by the crystallized garnet at the M1 stage. These graphite trails are likely the result of the interplay between surface energy and growth kinetics³⁰, whereby a growing garnet porphyroblast may displace the graphite instead of incorporating it until the graphite trail becomes too large to displace, and only then is the trail included. In conclusion, the second hypothesis (graphitization) is considered to be the most feasible one for the formation of graphite in the studied pelitic schists.

Subduction of sedimentary organic carbon to more than 90 km depths. The transport and storage of organic carbon during subduction processes can substantially impact the global carbon cycle and climate regulation^{6,8}. In this work, the characteristic of the light organic carbon isotopic composition (Fig. 4 and Supplementary Data 2) implies that the material source of pelitic schists-hosted graphite is surface-derived organic matter. The coexistence of coesite and graphite in garnet crystal (Fig. 2a–d) indicates the presence of graphite under the coesite stability field, which is at pressures exceeding 2.8 GPa when temperatures higher than 500 °C (see the Qz-to-Coe phase transition in Fig. 3a), but lower than the diamond stability field. Therefore, it can be proposed that the surface-derived organic

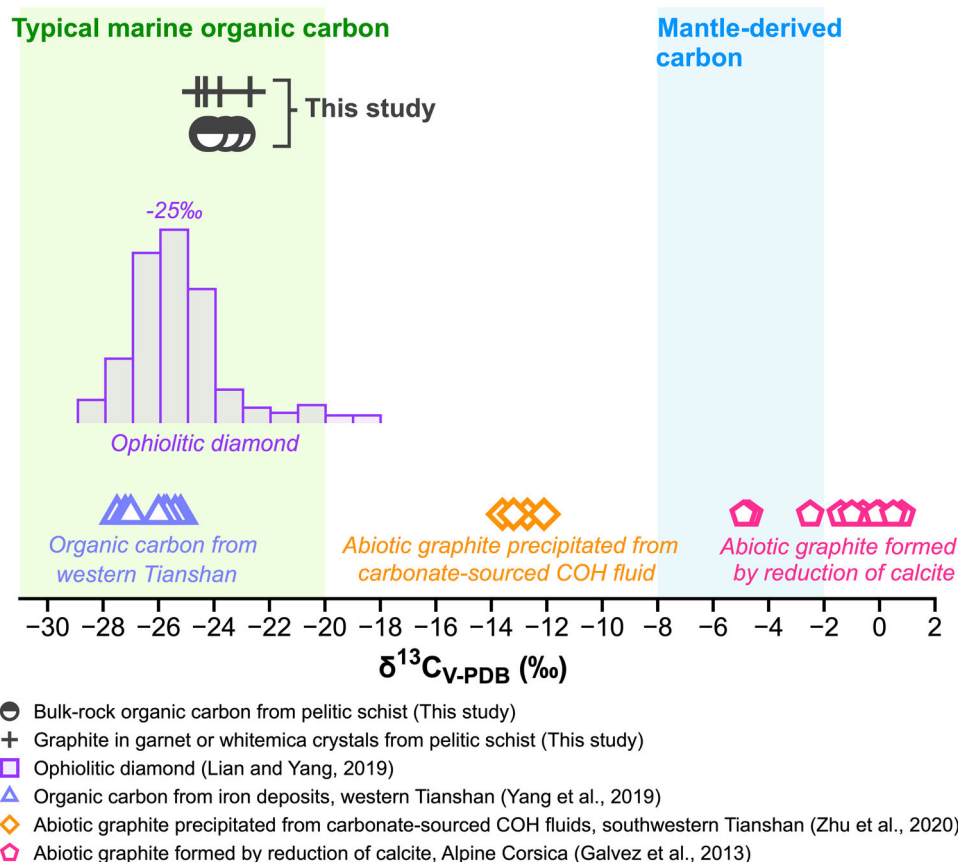


Fig. 4 $\delta^{13}\text{C}$ values (versus Pee Dee Belemnite standard) of bulk rock organic carbon and graphite contained in garnet and whitemica crystals from the coesite- and graphite-bearing pelitic schists in the Chinese southwestern Tianshan UHP metamorphic belt. For comparison, $\delta^{13}\text{C}_{\text{TOC}}$ (TOC, total organic carbon) values of abiotic graphite formed at HP conditions in subduction zones^{24, 25}, mantle-derived carbon¹⁸, typical marine organic carbon²⁰, organic carbon from iron deposits from western Tianshan²², and ophiolitic diamond³³ are also plotted.

matter was transported to subarc depths (>90 km) along with the oceanic slab.

Implication for diamond genesis. Diamond, a high-pressure polyphase of graphite, is estimated to be formed in the lithospheric mantle at depths exceeding 140 km or under pressures greater than 4.5 GPa³¹. An intriguing debate related to crustal recycling into the deep mantle regards the involvement of subduction-derived C in the genesis of diamond³². According to the literatures, some diamonds exhibit lighter carbon isotope characteristics (i.e., lower than mantle range)^{10,11}, particularly ophiolitic diamonds, which show $\delta^{13}\text{C}$ ranging from -29‰ to -18‰ with a peak value of -25‰ ^{9,33} (Fig. 4). Various theories have been posited to explain the light $\delta^{13}\text{C}$ compositions of these diamonds, including the primordial carbon reservoir, intramantle isotopic fractionation, or the incorporation of subducted biogenic/organic carbon³². However, mantle Sr, Nd, and O isotopic geochemistry data rule out the preservation of primordial carbon isotope heterogeneity in Earth's mantle. Moreover, the narrow range of $\delta^{13}\text{C}$ values from individual diamonds does not support isotope fractionation from a normal mantle carbon source with $\delta^{13}\text{C}$ of $-5 \pm 2\text{‰}$ ³². Therefore, the light carbon recorded by ophiolitic diamonds possibly reflects the composition of subducted organic carbon. However, the lack of robust petrological evidence makes this hypothesis arguable.

The results of this investigation have important implications for our understanding of the organic carbon cycle in the deep Earth and may inform ongoing debates concerning the origin and formation of diamonds with lower $\delta^{13}\text{C}$ values. Our study

provides the petrological evidence for the subduction of surface-derived organic carbon to the mantle depths of approximately 90 km, with the formation of graphitized organic carbon (graphite). Because diamonds can be formed by direct conversion from graphite within the diamond stability field³⁴, we propose that the continued subduction of this graphitized organic carbon may contribute to the formation of diamonds with light carbon isotope composition. This possible process can be inferred from the consistent C isotopic signatures between the ophiolitic diamond and organic carbon-sourced graphite (Fig. 4).

We conclude that, with the increasing subduction depth, surface-derived disordered organic carbon transformed to crystallized graphite at subarc depth (around 90 km) and subsequently to diamonds at lithospheric mantle depth (140 km), as illustrated in Fig. 5. Further studies are needed to fully elucidate the mechanisms and processes involved in the transition from surface organic carbon to graphite and then to diamonds.

Implication for the Lomagundi Event. The Lomagundi event, occurring around 2.3–2.0 billion years ago (Ga), was marked by a notable positive C isotope excursion of marine carbonates, with an increase of $\sim 10\text{‰}$ ³⁵. This event has been attributed to a variety of factors, including changes in the biogeochemical cycling of carbon³⁶, enhanced organic carbon burial^{6,7,37–40}, and increased volcanic outgassing^{7,37}.

In recent years, the deep subduction of organic carbon has emerged as a potential driver of the Lomagundi event, drawing considerable attention. Experimental and thermodynamic studies, along with the Carbon-oxygen box model^{6,7} all support this

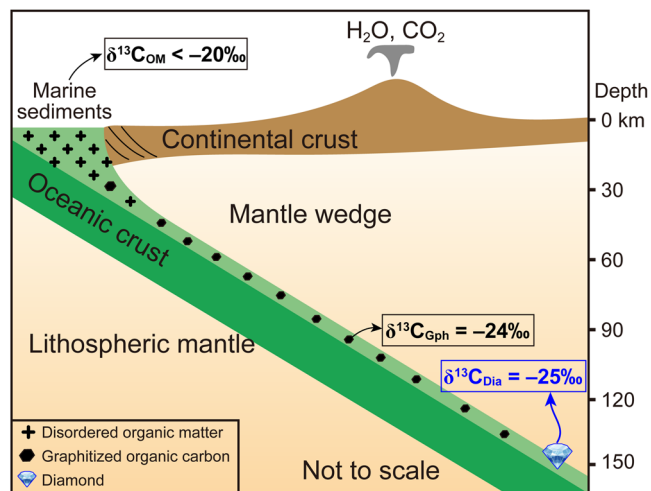


Fig. 5 Cartoon illustrating the fate of organic matter in subduction zones.

Disordered organic matter (OM) ($\delta^{13}\text{C}_{\text{OM}} < -20\text{‰}$) contained in marine sediments undergoes partial to complete graphitization with increasing temperature in subduction zones. The results presented in this study suggest that these disordered organic matter from marine sediments subducted to subarc depths (around 90 km, coesite-stable field), forming graphite with $\delta^{13}\text{C}_{\text{Gph}}$ of -24‰ . This subduction of surface organic carbon may contribute to the formation of ophiolitic diamonds with light $\delta^{13}\text{C}$ values (peak value of -25‰).

mechanism. This proposed process emphasizes the deep cycling of subducted organic carbon, which is deposited on the seafloor and subsequently subducted into the Earth's interior along with carbonates. Following subduction, organic carbon can be metamorphosed to graphite, which is more refractory than carbonate. At subarc conditions, carbonates are preferentially released from the slab over graphitized organic carbon, leading to an increase in arc volcano $\delta^{13}\text{C}$ values above -5‰ . Meanwhile, graphitized organic carbon remains in the slab and is transported deep into the mantle, where it may become entrained in upwelling mantle plumes feeding ocean island volcanoes. Reduced organic carbon in the upwelling plume is likely to undergo redox melting, resulting in a decrease in ocean island volcano $\delta^{13}\text{C}$ values to below -5‰ ⁷. In comparison to the subduction process (especially the carbonate-releasing process), the delayed eruption of the mantle plume resulted in a decrease in atmospheric $\delta^{13}\text{C}$ values. This decline subsequently contributed to a return of the $\delta^{13}\text{C}$ values of deposited marine carbonates to normal levels ($\sim 0\text{‰}$) after undergoing a large positive spike in carbon isotope ratios.

Our study offers petrological evidence to support the subduction of organic carbon to mantle depths, implying a plausible contribution of this process to the Lomagundi event's positive shift in carbon isotopic composition. These findings underscore the importance of considering the deep cycling of subducted organic carbon for understanding the mechanisms driving notable changes in biogeochemical cycles of carbon over geological timescales.

Methods

Mineral chemistry. Mineral major element compositions were analyzed with a JEOL 8230 electron probe microanalysis (EPMA) at the School of Earth and Space Sciences (SESS), Peking University, China. Synthetic silica (Si) and spessartine (Mn), natural sanidine (K), pyrope (Mg), andradite (Fe and Ca), albite (Na and Al), and rutile (Ti) served as standards for EPMA calibration. The acceleration voltage and beam current were 15 kV and 10 nA,

respectively. The beam diameter was 2 μm for silicates, and the counting times were 10–15 s. The PRZ correction was performed at the final calibration stage.

Raman spectroscopy. Raman spectra of coesite and graphite were acquired using a HORIBA Jobin Yvon confocal LabRAM HR Evolution micro-Raman system at the SESS, Peking University, China. The green laser (wavelength of 532 nm) was focused on the polished thin section with a 100 \times objective. The laser spot size was focused to 2 μm , and the laser power was 100 mW at the source, 1% (1 mW) for graphite, and 100% (100 mW) for silicate inclusions. Before each session, the spectrometer was calibrated using synthetic silicon (520.7 cm^{-1}). We selected graphite grains below the transparent adjacent/including mineral. Acquisition times varied from 10 to 20 s for coesite and from 20 to 40 s for graphite.

Organic carbon isotope and organic carbon concentration. For each analyzed sample, three types of powders (bulk-rock powder, garnet powder, and muscovite powder) were prepared for the carbon isotope ratio and concentration of graphite. The selected samples were washed with deionized water after removing the weathered surfaces. After crushing the samples into small fragments, clean pieces free of cracks and veins were handpicked. Then these pieces were powdered in an agate mortar to make the bulk-rock powder (<200 mesh). Graphite-bearing garnet crystals and graphite-bearing muscovite crystals were handpicked respectively from the bulk-rock powder and were powdered to make the garnet powder (<200 mesh) and the muscovite powder (<200 mesh). All Powders were treated with 1 mol/L HCl to remove carbonate, and the acid-insoluble fraction was then rinsed with distilled water and dried at 60 $^{\circ}\text{C}$ in an oven for 24 h.

Total organic carbon (TOC) concentrations and isotopic composition ($\delta^{13}\text{C}$) measurements were carried out by using the Thermo Scientific EA IsoLink Isotope Ratio Mass Spectrometer (IRMS) System at the SESS, Peking University, China. Dried, carbonate-free samples were wrapped in tin capsules and placed in the EA autosampler. Then the samples were dropped into the cleaned quartz tubes and sealed under vacuum for combustion and oxidation with CuO (1100 $^{\circ}\text{C}$) for carbonaceous matter (CM) extraction. The generated gases (N_2 and CO_2) were separated on a chromatographic column, and the carbon isotopic composition of the separated CO_2 was then measured with a Thermo Scientific Delta V Advantage continuous flow isotope ratio mass spectrometer. Empty muffled tin capsules were run for contamination before analysis, and no carbon was detected in these procedural blank tin capsules. To minimize external and internal uncertainties, calibration standards urea (IVA3380217, $\delta^{13}\text{C} = -40.8\text{‰}$), GBW04406 (CaCO_3 , $\delta^{13}\text{C} = -10.85\text{‰}$), USGS24 (graphite, $\delta^{13}\text{C} = -16.05\text{‰}$), USGS44 (CaCO_3 , $\delta^{13}\text{C} = -42.21\text{‰}$), IAEA-CO-8 (CaCO_3 , $\delta^{13}\text{C} = -5.76\text{‰}$), IAEA-603 (CaCO_3 , $\delta^{13}\text{C} = +2.465\text{‰}$), and NBS18 (CaCO_3 with a $\delta^{13}\text{C}$ value of -5.01‰) were systematically run during the measurements. $\delta^{13}\text{C}$ values were normalized to the V-PDB (versus Pee Dee Belemnite) standard. Based on duplicate standards, the $\delta^{13}\text{C}$ analytical precision was better than 0.2‰, and the carbon concentration analytical precision was better than 0.05%.

Phase equilibrium modeling. Phase equilibrium modeling was conducted in the system of $\text{Na}_2\text{O}-\text{CaO}-\text{K}_2\text{O}-\text{FeO}-\text{MgO}-\text{Al}_2\text{O}_3-\text{SiO}_2-\text{H}_2\text{O}-\text{TiO}_2-\text{CO}_2$ (NCKFMASHTi+ CO_2) using the XRF bulk composition (Supplementary Data 3) with the measured CO_2 content, and H_2O and SiO_2 in excess for sample H1813B. It is generally accepted that subducted sediments

underwent restricted decarbonation during subduction metamorphism along low-temperature geotherms⁴¹. Therefore, the measured CO₂ content is the total CO₂ content of the modeling system. We modified the bulk composition to assume apatite saturation by removing P₂O₅ and the corresponding CaO using a P/Ca molar ratio of 3/5. The P–T diagrams were calculated with *Perple_X*^{42,43} and the thermodynamic database (*hp62ver.dat*)⁴⁴. Mineral solid solution models were: (i) Gt(W) for garnet, Mica(W) for white mica, Chl(W) for chlorite, Ctd(W) for chloritoid⁴⁵, (ii) cAmph(G) for amphibole, Omph(GHP) for omphacite⁴⁶, (iii) feldspar for feldspar⁴⁷, (iv) Carp(M) with two endmembers (Mg–Fe) for carpholite⁴⁸, (v) F for H₂O–CO₂ fluid solution⁴⁹, (vi) oCcM(EF) for carbonate⁵⁰. Pure endmember phases included zoisite, lawsonite, quartz/coesite, ankerite, aragonite, rutile, ilmenite, and titanite.

Data availability

The dataset used in this study are available at <https://doi.org/10.6084/m9.figshare.24416572> (last access: 21 October 2023).

Received: 6 August 2023; Accepted: 6 November 2023;

Published online: 16 November 2023

References

1. Ague, J. J. & Nicolescu, S. Carbon dioxide released from subduction zones by fluid-mediated reactions. *Nat. Geosci.* **7**, 355–360 (2014).
2. Kelemen, P. B. & Manning, C. E. Reevaluating carbon fluxes in subduction zones, what goes down, mostly comes up. *Proc. Natl. Acad. Sci. USA* **112**, E3997–E4006 (2015).
3. Plank, T. & Manning, C. E. Subducting carbon. *Nature* **574**, 343–352 (2019).
4. Sverjensky, D. A., Stagno, V. & Huang, F. Important role for organic carbon in subduction-zone fluids in the deep carbon cycle. *Nat. Geosci.* **7**, 909–913 (2014).
5. Frezzotti, M. L. Diamond growth from organic compounds in hydrous fluids deep within the Earth. *Nat. Commun.* **10**, 4952 (2019).
6. Duncan, M. S. & Dasgupta, R. Rise of Earth's atmospheric oxygen controlled by efficient subduction of organic carbon. *Nat. Geosci.* **10**, 387–392 (2017).
7. Eguchi, J., Seales, J. & Dasgupta, R. Great Oxidation and Lomagundi events linked by deep cycling and enhanced degassing of carbon. *Nat. Geosci.* **13**, 71–76 (2020).
8. Tumiati, S. et al. Subducted organic matter buffered by marine carbonate rules the carbon isotopic signature of arc emissions. *Nat. Commun.* **13**, 2909 (2022).
9. Yang, J., Wu, W., Lian, D. & Rui, H. Peridotites, chromitites and diamonds in ophiolites. *Nat. Rev. Earth Environ.* **2**, 198–212 (2021).
10. Cartigny, P., Palot, M., Thomassot, E. & Harris, J. W. Diamond formation: a stable isotope perspective. *Annu. Rev. Earth Planet. Sci.* **42**, 699–732 (2014).
11. Schulze, D. J. et al. Anticorrelation between low $\delta^{13}\text{C}$ of eclogitic diamonds and high $\delta^{18}\text{O}$ of their coesite and garnet inclusions requires a subduction origin. *Geology* **41**, 455–458 (2013).
12. Giuliani, A. et al. Perturbation of the deep-Earth carbon cycle in response to the Cambrian Explosion. *Sci. Adv.* **8**, eabj1325 (2022).
13. Lü, Z., Zhang, L. F., Du, J. X. & Bucher, K. Coesite inclusions in garnet from eclogitic rocks in western Tianshan, northwest China: convincing proof of UHP metamorphism. *Am. Mineral.* **93**, 1845–1850 (2008).
14. Yang, X., Zhang, L., Tian, Z. & Bader, T. Petrology and U–Pb zircon dating of coesite-bearing metapelite from the Kebuete Valley, western Tianshan, China. *J. Asian Earth Sci.* **70–71**, 295–307 (2013).
15. Valley, J. W. & O'Neil, J. R. ¹³C/¹²C exchange between calcite and graphite: a possible thermometer in Grenville marbles. *Geochim. Cosmochim. Acta* **45**, 411–419 (1981).
16. Wada, H. Microscale isotopic zoning in calcite and graphite crystals in marble. *Nature* **331**, 61–63 (1988).
17. Schidlowski, M. Carbon isotopes as biogeochemical recorders of life over 3.8 Ga of Earth history: evolution of a concept. *Precambrian Res.* **106**, 117–134 (2001).
18. Luque, F. J., Crespo-Feo, E., Barrenechea, J. F. & Ortega, L. Carbon isotopes of graphite: implications on fluid history. *Geosci. Front.* **3**, 197–207 (2012).
19. Luque, F. J., Pasteris, J. D., Wopenka, B., Rodas, M. & Barrenechea, J. F. Natural fluid-deposited graphite: Mineralogical characteristics and mechanisms of formation. *Am. J. Sci.* **298**, 471–498 (1998).
20. Hoefs, J. *Stable Isotope Geochemistry* 6th (Springer Berlin, Heidelberg, 2009).
21. Ray, J. S. Carbon isotopic variations in fluid-deposited graphite: evidence for multicomponent Rayleigh isotopic fractionation. *Int. Geol. Rev.* **51**, 45–57 (2009).
22. Yang, X. Q. et al. The carboniferous Shikebutai iron deposit in western Tianshan, northwestern China: petrology, Fe–O–C–Si isotopes, and implications for iron pathways. *Econ. Geol.* **114**, 1207–1222 (2019).
23. Luque, F. J. et al. Deposition of highly crystalline graphite from moderate-temperature fluids. *Geology* **37**, 275–278 (2009).
24. Galvez, M. E. et al. Graphite formation by carbonate reduction during subduction. *Nat. Geosci.* **6**, 473–477 (2013).
25. Zhu, J., Zhang, L., Tao, R. & Fei, Y. The formation of graphite-rich eclogite vein in S.W. Tianshan (China) and its implication for deep carbon cycling in subduction zone. *Chem. Geol.* **533**, 119430 (2020).
26. Etiope, G. & Sherwood Lollar, B. Abiotic methane on earth. *Rev. Geophys.* **51**, 276–299 (2013).
27. Buseck, P. R. & Beyssac, O. From organic matter to graphite: graphitization. *Elements* **10**, 42–426 (2014).
28. Beyssac, O., Goffé, B., Chopin, C. & Rouzaud, J. N. Raman spectra of carbonaceous material in metasediments: a new geothermometer. *J. Metamorph. Geol.* **20**, 859–871 (2002).
29. Beyssac, O. et al. On the characterization of disordered and heterogeneous carbonaceous materials by Raman spectroscopy. *Spectrochim. Acta Part A Mol. Biomol. Spectrosc.* **59**, 2267–2276 (2003).
30. Passchier, C. W., Trouw, R. A. *Microtectonics*. (Springer Science & Business Media, 2005).
31. Sobolev, N. V. et al. Fossilized high pressure from the Earth's deep interior: the coesite-in-diamond barometer. *Proc. Natl. Acad. Sci. USA* **97**, 11875–11879 (2000).
32. Cartigny, P. Stable isotopes and the origin of diamond. *Elements* **1**, 79–84 (2005).
33. Lian, D. & Yang, J. Ophiolite-hosted diamond: a new window for probing carbon cycling in the deep mantle. *Engineering* **5**, 406–420 (2019).
34. Tappert, R. et al. Subducting oceanic crust: the source of deep diamonds. *Geology* **33**, 565–568 (2005).
35. Bekker, A. et al. Fractionation between inorganic and organic carbon during the Lomagundi (2.22–2.1 Ga) carbon isotope excursion. *Earth Planet. Sci. Lett.* **271**, 278–291 (2008).
36. Mänd, K. et al. Palaeoproterozoic oxygenated oceans following the Lomagundi–Jatuli Event. *Nat. Geosci.* **13**, 302–306 (2020).
37. Eguchi, J., Diamond, C. W. & Lyons, T. W. Proterozoic supercontinent break-up as a driver for oxygenation events and subsequent carbon isotope excursions. *PNAS Nexus* **1**, pgac036 (2022).
38. Karhu, J. A. & Holland, H. D. Carbon isotopes and the rise of atmospheric oxygen. *Geology* **24**, 867–870 (1996).
39. Parnell, J. & Brolly, C. Increased biomass and carbon burial 2 billion years ago triggered mountain building. *Commun. Earth Environ.* **2**, 238 (2021).
40. Bekker, A. & Holland, H. Oxygen overshoot and recovery during the early Paleoproterozoic. *Earth Planet. Sci. Lett.* **317**, 295–304 (2012).
41. Kerrick, D. M. & Connolly, J. A. Metamorphic devolatilization of subducted marine sediments and the transport of volatiles into the Earth's mantle. *Nature* **411**, 293–296 (2001).
42. Connolly, J. A. D. The geodynamic equation of state: what and how. *Geochem. Geophys. Geosyst.* **10**, 10 (2009).
43. Connolly, J. A. D. Computation of phase equilibria by linear programming: A tool for geodynamic modeling and its application to subduction zone decarbonation. *Earth Planet. Sci. Lett.* **236**, 524–541 (2005).
44. Holland, T. J. B. & Powell, R. An improved and extended internally consistent thermodynamic dataset for phases of petrological interest, involving a new equation of state for solids. *J. Metamorph. Geol.* **29**, 333–383 (2011).
45. White, R., Powell, R., Holland, T., Johnson, T. & Green, E. New mineral activity–composition relations for thermodynamic calculations in metapelite systems. *J. Metamorph. Geol.* **32**, 261–286 (2014).
46. Green, E. C. R. et al. Activity–composition relations for the calculation of partial melting equilibria in metabasic rocks. *J. Metamorph. Geol.* **34**, 845–869 (2016).
47. Fuhrman, M. L. & Lindsley, D. H. Ternary-Feldspar modeling and thermometry. *Am. Mineral.* **73**, 201–215 (1988).
48. Massonne, H. J. & Willner, A. P. Phase relations and dehydration behaviour of psammopelite and mid-ocean ridge basalt at very-low-grade to low-grade metamorphic conditions. *Eur. J. Mineral.* **20**, 867–879 (2008).
49. Connolly, J. A. D. & Trommsdorff, V. Petrogenetic grids for metacarbonate rocks: pressure–temperature phase–diagram projection for mixed-volatile systems. *Contrib. Mineral. Petrol.* **108**, 93–105 (1991).
50. Franzolin, E., Schmidt, M. & Poli, S. Ternary Ca–Fe–Mg carbonates: subsolidus phase relations at 3.5 GPa and a thermodynamic solid solution model including order/disorder. *Contrib. Mineral. Petrol.* **161**, 213–227 (2011).

Acknowledgements

We thank Xiaoli Li, Ying Cui, and Yi Su for their help with EPMA, Raman, and isotopic analyses, respectively. We thank Thomas Bader for the discussion during the manuscript revision. We gratefully acknowledge editor Joe Aslin for the careful editorial handling and Dongyang Lian and an anonymous reviewer for the detailed and constructive comments. No permission was required to collect the samples during fieldwork. This work was funded by the National Basic Research Program of China (2019YFA0708501) and the National Natural Science Foundation of China (Grant No. 42202049).

Author contributions

L.Z. and H.H. designed the study, H.H., C.L., and Z.L. collected samples, and H.H. collected analytical data and wrote the original manuscript. L.Z. reviewed the manuscript.

Competing interests

The authors declare no competing interests.

Additional information

Supplementary information The online version contains supplementary material available at <https://doi.org/10.1038/s43247-023-01085-w>.

Correspondence and requests for materials should be addressed to Lifei Zhang.

Peer review information *Communications Earth & Environment* thanks Dongyang Lian and the other, anonymous, reviewer(s) for their contribution to the peer review of this

work. Primary Handling Editors: Joe Aslin, Heike Langenberg. Peer reviewer reports are available.

Reprints and permission information is available at <http://www.nature.com/reprints>

Publisher's note Springer Nature remains neutral with regard to jurisdictional claims in published maps and institutional affiliations.



Open Access This article is licensed under a Creative Commons Attribution 4.0 International License, which permits use, sharing, adaptation, distribution and reproduction in any medium or format, as long as you give appropriate credit to the original author(s) and the source, provide a link to the Creative Commons licence, and indicate if changes were made. The images or other third party material in this article are included in the article's Creative Commons licence, unless indicated otherwise in a credit line to the material. If material is not included in the article's Creative Commons licence and your intended use is not permitted by statutory regulation or exceeds the permitted use, you will need to obtain permission directly from the copyright holder. To view a copy of this licence, visit <http://creativecommons.org/licenses/by/4.0/>.

© The Author(s) 2023